Chemical Science

ROYAL SOCIETY OF CHEMISTRY

EDGE ARTICLE

View Article Online
View Journal

Cite this: DOI: 10.1039/d5sc08906a

All publication charges for this article have been paid for by the Royal Society of Chemistry

Frozen slab method mediated sulfur-affinitive single-atom catalysts for efficient reversible sodium storage

Kai Cui,†[a] Zijia Qi,†[b] Dominik Legut,[cd] Wanxiang Zhao,[e] Biao Chen,[b] Ningning Wu,*[fg] Qiuyu Zhang *[a] and Tianshuai Wang *[ah]

Carbon-supported single-atom catalysts (C-SAMs) have recently emerged as a frontier strategy to address the issue of irreversible reactions in MoS_2-based sodium-ion batteries. However, conventional C-SAMs designed solely considering the d–p orbital coupling theory often yield distorted adsorption energy predictions for Na_2S, as it overlooks the roles of Na–N bond interactions and structural deformation. Herein, we introduce the frozen slab method to evaluate the influence of C-SAMs' affinities toward Na and S on Na_2S adsorption. Based on their relative adsorption strengths, C-SAMs are classified into three categories: S-affinitive, amphiphilic, and Na-affinitive. Theoretical calculations reveal that S-affinitive C-SAMs strongly adsorb S atoms, thereby weakening the Na–S bond in Na_2S and facilitating bond cleavage during charging. This reduces the decomposition energy barrier of Na_2S and enhances the reversibility of the conversion reaction. Experimental results confirm that S-affinitive C-SAV can accelerate Na^+ storage kinetics in MoS_2, enabling highly efficient reversible conversion during charging. As a result, after 1000 cycles at a high current density of 5 A g^{-1}, the MoS_2/C-SAV electrode exhibits a specific capacity of 332.8 mAh g^{-1}, with a capacity retention rate as high as 98.87% and an average capacity decay of only 0.001% per cycle.

Received 14th November 2025
Accepted 21st December 2025

DOI: 10.1039/d5sc08906a

rsc.li/chemical-science

Introduction

Sodium-ion batteries (SIBs) are regarded as a promising technology for large-scale energy storage owing to the earth-abundant sodium resources, low cost, and compatibility with most existing lithium-ion battery (LIB) manufacturing infrastructure.[1–5] Although graphite has been successfully employed as the anode material in commercial LIBs, it is unsuitable for sodium storage due to the much larger ionic radius of Na (1.02 Å for Na^+ *vs.* 0.76 Å for Li^+).[6–9] This larger ionic radius, coupled with the higher molar mass of Na, leads to sluggish reaction kinetics during Na^+ insertion and extraction and pronounced volume changes in most anodes.[10–13] These intrinsic limitations pose significant challenges for the design and development of high-performance, cost-effective anodes for SIBs.[14]

In addition to conventional layered materials that store sodium *via* an insertion/extraction mechanism, conversion-type anode materials—particularly transition metal sulfides such as MoS_2—are considered highly promising candidates for SIBs.[15–19] This is mainly attributed to their unique layered structure, which facilitates Na^+ diffusion, and their high theoretical capacity (664 mAh g^{-1}) derived from a four-electron transfer conversion reaction.[20–22] Nevertheless, achieving highly reversible conversion reactions with MoS_2 remains challenging due to severe structural pulverization during discharge, along with the intrinsically insulating nature and high decomposition barrier of agglomerated Na_2S.[23] As a result, an irreversible conversion process frequently occurs, producing Mo and S instead of the original MoS_2 after the first cycle, which in turn leads to pronounced electrochemical polarization and rapid capacity fading, primarily due to the notorious shuttle effect associated with the Na–S storage mechanism.[24–27]

To boost the reversible degree of the conversion reaction of MoS_2 during repeated cycling, extensive research efforts have

[a]School of Chemistry and Chemical Engineering, Northwestern Polytechnical University, Xi'an, 710129, P.R. China. E-mail: qyzhang@nwpu.edu.cn; tianshuai@nwpu.edu.cn

[b]School of Materials Science and Engineering, Tianjin University, Tianjin, 300350, P. R. China

[c]IT4Innovations, VSB-Technical University of Ostrava, 17. listopadu 2172/15, 708 00 Ostrava, Czech Republic

[d]Department of Condensed Matter Physics, Faculty of Mathematics and Physics, Charles University, Ke Karlovu 3, 121 16 Prague 2, Czech Republic

[e]Suzhou Nuclear Power Research Institute, Suzhou 215004, China

[f]School of Materials Science & Engineering and State Key Laboratory of Reliability and Intelligence of Electrical Equipment, P.R. China. E-mail: wuningning69@139.com

[g]School of Electrical Engineering, Hebei University of Technology, Tianjin 300401, P. R. China

[h]Chongqing Science and Technology Innovation Center of Northwestern Polytechnical University, Chongqing 401135, P. R. China

† Kai. Cui and Zijia Qi contributed equally to this work.

been devoted in recent years.[28,29] Among various strategies, compositing MoS_2 with highly conductive carbon materials has been demonstrated to effectively shorten the Na^+ transport pathway through interfacial effects, thereby improving reaction kinetics and, to some extent, enhancing the reversible capacity ratio.[30,31] Fundamentally, achieving a higher reversible capacity requires fully reversible decomposition of the Na_2S/Mo composite, weakening the Na–S bond and facilitating subsequent reaction kinetics. Incorporating single-atom materials into MoS_2 has emerged as an effective approach, owing to their high electrical conductivity, superior catalytic activity, and large specific surface area. The catalytic metal centers in single-atom materials can couple their d orbitals with the p orbitals of S in Na_2S, thereby weakening the Na–S bond and accelerating the following reaction kinetics ($Mo/Na_2S \rightarrow NaMoS_2 \rightarrow MoS_2$).[26] Since Chen *et al.* first introduced single-atom Fe into MoS_2 in 2021 to improve its reversible capacity,[23] a variety of single-atom materials such as SAMn,[32] SANi,[33] and SACo[34] have been developed and successfully applied to MoS_2-based single-atom composites, achieving notable enhancements in electrochemical performance.

Nevertheless, identifying the optimal metal catalytic center remains an open task. Previous studies have predominantly relied on the d–p orbital coupling theory to evaluate the interaction between single-atom materials and Na_2S, thereby inferring their catalytic activity.[35–37] However, recent findings reveal that the coordinated nitrogen atoms in single-atom materials also play a crucial role in catalysis, as they can influence the interaction with Na_2S through the formation of N–Na bonds.[38–40] Therefore, the selection of single-atom materials should consider the synergistic effects of both the metal center and the coordinated nitrogen. It can be anticipated that variations in the metal center will modulate the electronic structure of the coordinated nitrogen, leading to changes in the affinity of single-atom materials toward Na and S in Na_2S. Based on their relative affinities for S and Na, single-atom materials can be categorized into S-affinitive, amphiphilic, and Na-affinitive types. Determining which category delivers the most effective catalytic performance remains an important scientific endeavour that warrants further investigation.

Herein, we propose for the first time a classification of nine types of carbon-supported single-atom catalysts (C-SAMs, M = Sc, Ti, V, Cr, Mn, Fe, Co, Ni, Cu, Zn) into S-affinitive, amphiphilic, and Na-affinitive categories based on their relative affinities for S and Na. Using the frozen slab method (FSM)—rather than the conventional method (CM)—to calculate adsorption energies, we reevaluated their catalytic effects on Na_2S decomposition and their ability to enhance the reaction reversibility of MoS_2.[41] Theoretical results demonstrate that S-affinitive C-SAMs can strongly adsorb Na_2S, weakening Na–S bonds and facilitating their dissociation during charging, thereby reducing the decomposition energy barrier of Na_2S on C-SAM surfaces. As a result, the capacity retention rate of MoS_2/S-affinitive C-SAV is as high as 98.87%, corresponding to an ultralow capacity decay rate of merely 0.001% per cycle, indicating that the S-affinitive C-SAV catalyst effectively promotes the reversible conversion reaction of MoS_2 and endows MoS_2 with extremely long-cycle stability. Moreover, leveraging interpretable machine learning, we further propose physical structure descriptors centered on single-atom sites to predict the catalytic strategies for promoting Na_2S decomposition, thereby offering valuable guidance for the development of highly reversible MoS_2-based anode materials.

Results and discussion

First, we classified S-affinitive, amphiphilic, and Na-affinitive catalysts based on a comparative analysis of their adsorption energies toward sodium and sulfur atoms. When the adsorption energy for sulfur atoms is greater than that for sodium atoms, we consider the metal center to play the dominant role in Na_2S adsorption, thereby categorizing the catalyst as S-affinitive. Conversely, when the adsorption energy for sulfur atoms is lower than that for sodium atoms, we attribute the primary role in Na_2S adsorption to the nitrogen atoms, classifying the catalyst as Na-affinitive. When the adsorption energies for sulfur and sodium are comparable, both the metal center and the coordinated nitrogen atoms contribute similarly to Na_2S adsorption, and the catalyst is defined as the amphiphilic type. By analyzing the metal d-band centers and the p-band centers of coordinated nitrogen for nine types of single-atom catalysts (Table S1), we found that the p-band center of the coordinated nitrogen varies with the type of central metal, thereby influencing the affinity toward sodium. Subsequently, we calculated the adsorption energies of Na, S, and Na_2S on the nine types of C-SAMs with $M–N_4$ (M = Sc, Ti, V, Cr, Mn, Fe, Co, Ni, Cu, Zn) active centers, as illustrated in Fig. 1a, S1–S4 and Tables S2–S3.

Notably, during the adsorption calculation processes, we observed that the metal centers of the C-SAMs exhibited varying degrees of displacement toward the adsorbates, and the initial configuration could not spontaneously recover after desorption (Fig. S2–S4). This indicates that the C-SAMs transition from one stable state to another during adsorption, accompanied by energy changes. Consequently, structural changes of the C-SAMs during adsorption will influence the calculation of adsorption energies. To account for the impact of C-SAM structural changes, we introduced the FSM to reevaluate the adsorption energy of adsorbates. To quantitatively evaluate the efficacy of this method, we employed integrated crystal orbital Hamilton population (ICOHP) analysis. ICOHP comprehensively combines the positive and negative contributions of bonding and antibonding states, enabling the quantification of additional effects arising from surface structural relaxation during molecular adsorption on C-SAMs.[42] Thus, ICOHP can assess the role of the FSM in improving the accuracy of density functional theory (DFT) predictions. Given that S exerts a significant and relatively direct influence on metal atoms, we calculated all the adsorption energies, frozen slab adsorption energies of S on C-SAMs and the ICOHP values of metal–sulfur (M–S) bonds to elucidate the effect of C-SAM deformation on adsorption energy. As shown in Tables S2–S4, the frozen slab adsorption energies exhibit a stronger linear correlation with the ICOHP values of the M–S bonds compared to those obtained from conventional methods, indicating that the frozen slab

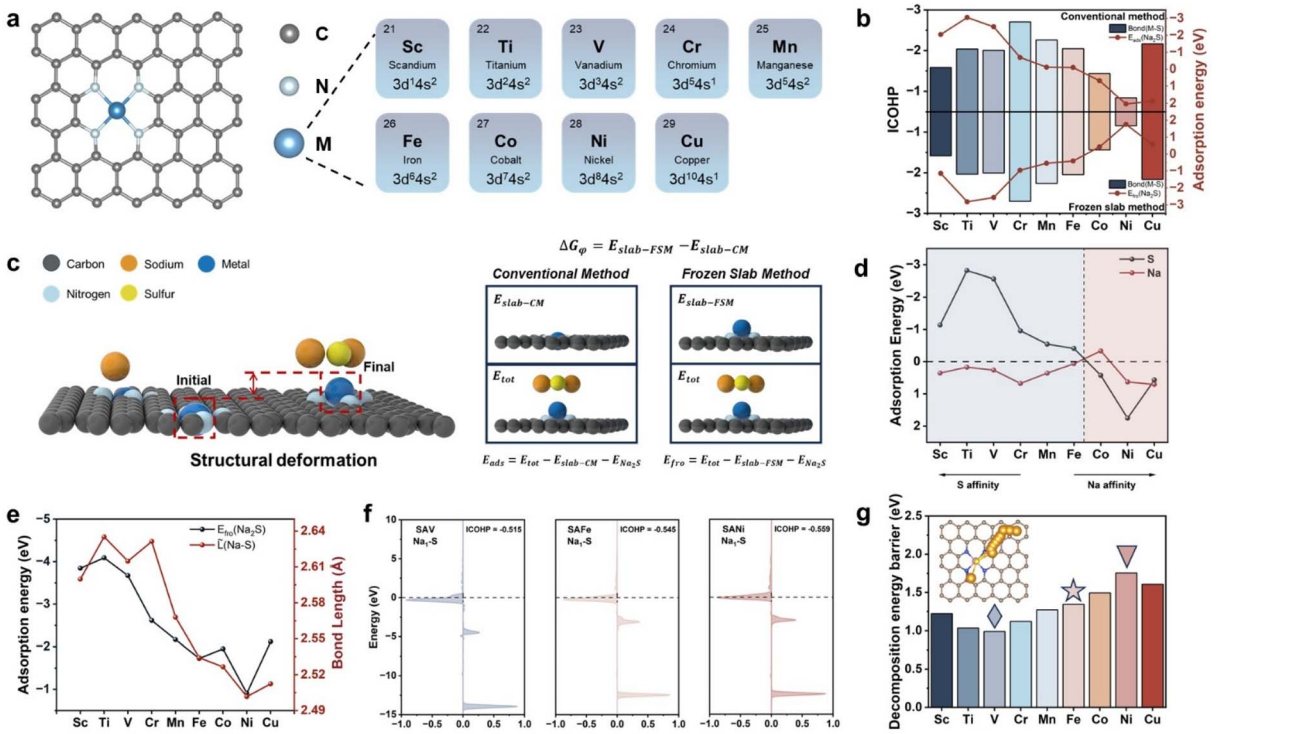

Fig. 1 (a) Schematic structure of the C-SAMs. (b) The strength of M–S bonds between C-SAMs and S evaluated by ICOHP and the adsorption energies of C-SAMs for S evaluated by the conventional method and frozen slab method. (c) Diagram of the frozen slab method. (d) The frozen slab adsorption energies of the C-SAMs for Na and S. (e) The frozen slab adsorption energies of C-SAMs for Na_2S and the length of the Na–S bonds in Na_2S when C-SAMs adsorb Na_2S. (f) The strength of Na–S bonds in Na_2S when C-SAV, SAFe and SANi adsorb Na_2S evaluated by ICOHP. (g) The decomposition energy barriers of Na_2S on C-SAMs.

method is beneficial for distinguishing C-SAMs with superior catalytic performance. We also noted that the C-SAMs do not spontaneously revert to their initial configuration after the removal of the adsorbed S atoms (Fig. S1). Concurrently, significant structural deformation induces changes in the electronic structure of the C-SAMs, leading to a shift in the d-band center of the metal atoms. As shown in Fig. S5 and Table S1, the d band centers change most significantly in C-SAMs with pronounced structural deformation, such as C-SASc, C-SATi, and C-SACu.

Additionally, considering the significance of Na_2S adsorption on C-SAMs, we also calculated the ICOHP values of the M–S bonds during the adsorption of Na_2S on C-SAMs. As shown in Fig. 1b, the energy contributions from structural deformation during Na_2S adsorption vary considerably among different C-SAMs. After correction, the linear correlation between M–S bond strength and the adsorption energies of Na_2S on the catalysts was enhanced. This suggests that excluding the energy arising from C-SAM structural deformation yields results closer to the actual scenario. Based on the above, we exclude strain energy (ΔG_φ) caused by C-SAM structural deformation when calculating adsorption energies. The specifics of the FSM are depicted in Fig. 1c. In the CM, the adsorption energy (E_{ads}) is calculated as the total energy (E_{tot}) minus the sum of the pre-adsorption substrate energy and the adsorbate energy. In the FSM, the ΔG_φ arising from the structural deformation of C-SAMs during the adsorption process is explicitly accounted for. Thus, the corrected frozen slab adsorption energy (E_{fro}) is calculated as E_{tot} minus the sum of the post-adsorption substrate energy and the adsorbate energy, or equivalently, as the E_{ads} minus the ΔG_φ. After correcting the adsorption energies using the FSM, we observed significant differences in the adsorption strengths of different C-SAMs for Na and S. Fig. 1d displays the adsorption energies of various C-SAMs for Na and S atoms. Based on the relative adsorption strengths for S and Na, we categorized the C-SAMs into three groups: (1) C-SAMs with low d-electron counts (Sc, Ti, and V) exhibit significantly stronger adsorption for S than for Na, classifying them as S-affinitive C-SAMs; (2) C-SAMs with intermediate d-electron counts (Cr, Mn, and Fe) show comparable interactions with S and Na, classifying them as amphiphilic C-SAMs; (3) C-SAMs with high d-electron counts (Co, Ni, and Cu) exhibit significantly stronger adsorption for Na than for S, classifying them as Na-affinitive C-SAMs.

Given that the decomposition of Na_2S plays a critical role in the Mo/Na_2S → $NaMoS_2$ charging process, we further analyzed the adsorption behavior of the three categorized C-SAMs toward Na_2S. As shown in Fig. 1e, the frozen slab adsorption energies of Na_2S on C-SAMs gradually weaken with the increasing atomic number of the central metal atom. Moreover, the Na–S bond length in the adsorbed Na_2S configurations exhibits a strong linear correlation with adsorption energy (Fig. 1e): stronger

Na_2S adsorption is accompanied by longer Na–S bonds. We speculate that this is because the adsorption of Na_2S on C-SAMs primarily arises from the M–S bond. Thus, stronger adsorption energies indicate stronger coupling between the d-orbitals of the C-SAM's metal atom and the p-orbitals of S in Na_2S, thereby weakening the interaction between S and Na in Na_2S, leading to elongated Na–S bonds, making them more susceptible to dissociation during the charging process. To quantify the strength of Na–S bonds, we calculated their ICOHP values. As shown in Fig. 1f and Table S5, the Na–S bond strength is generally the weakest in S-affinitive C-SAMs (−0.497 to −0.519), indicating a pronounced weakening effect, while Na-affinitive C-SAMs exhibit the strongest Na–S bonds (C-SACo: −0.523 and C-SANi: −0.562), suggesting a relatively smaller weakening effect. Amphiphilic C-SAMs exhibit intermediate weakening effects. Based on these observations, we hypothesized that the decomposition energy barrier of Na_2S is lower on S-affinitive C-SAMs and higher on Na-affinitive C-SAMs. To confirm our predictions, climbing image nudged elastic band calculations were performed to calculate the decomposition barriers of Na_2S ($E_{bar}(Na_2S)$) on various C-SAM surfaces. As shown in Fig. 1g, the $E_{bar}(Na_2S)$ are indeed lower on S-affinitive C-SAMs and higher on Na-affinitive C-SAMs, with amphiphilic C-SAMs exhibiting intermediate barriers. Specifically, Na_2S exhibits the lowest decomposition barrier on C-SAV (0.989 eV) and the highest on C-SANi (1.755 eV). These results demonstrate that S-affinitive C-SAMs can strongly adsorb Na_2S, weakening Na–S bonds and facilitating their dissociation during charging, thereby reducing the decomposition energy barrier of Na_2S on C-SAM surfaces.

Building on our previous work demonstrating that purely physical descriptors can effectively predict catalyst activity and guide catalyst design at reduced screening costs, we applied the Sure Independence Screening and Sparsifying Operator (SISSO) to derive physical descriptors to describe the $E_{bar}(Na_2S)$ on the different C-SAMs.[43–45] The feature extraction process is illustrated in Fig. 2b. We first obtained atomic features from three open databases: Villars, Magpie, and Mendeleev. Subsequently, through a three-step procedure "removal of duplicates → Pearson selection → manual screening", we identified 11 physical features that exhibited a correlation below 0.8 with the

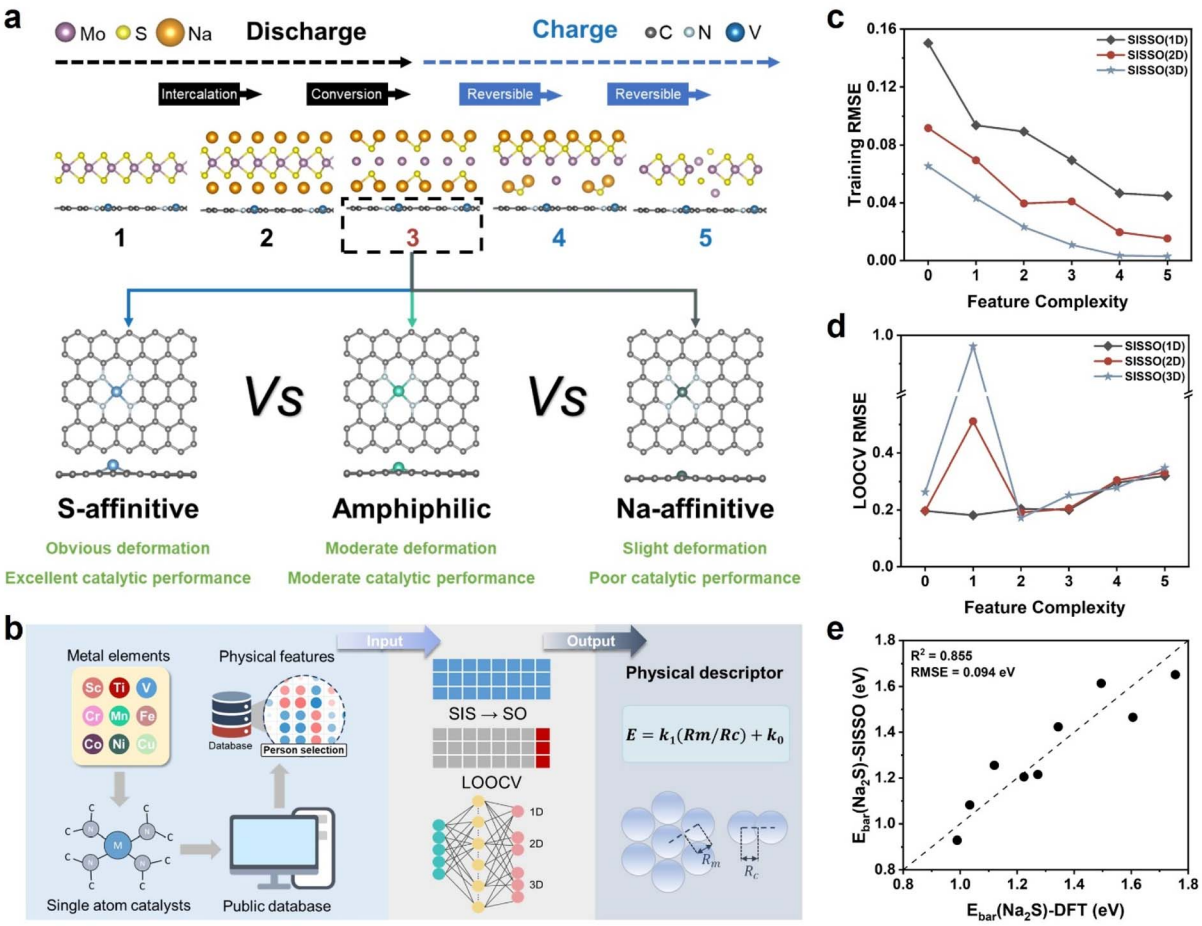

Fig. 2 (a) Illustration of the reversible reaction pathway during discharge and charging processes for the three categories of C-SAMs. (b) A flowchart of the SISSO approach combined with high-throughput DFT calculations to identify physical descriptors for predicting the performance of catalysts. (c) Relationship between training RMSE and feature complexity for the models in different dimensions. (d) Prediction errors of RMSE for the models in different dimensions obtained by SISSO repeated LOOCV. (e) SISSO 1D descriptor prediction results of $E_{bar}(Na_2S)$ compared with the results obtained from DFT calculations.

$E_{bar}(Na_2S)$ and did not require DFT calculations. These features included the electronegativity, first ionization energy, and atomic radius of the metal atoms, along with other characteristics listed in Table S6.

Using the SISSO, we performed mathematical operations across multiple dimensions to fit precise formulae for the $E_{bar}(Na_2S)$ on all C-SAMs. This yielded highly accurate and generalizable descriptors. The prediction results, shown in Fig. 2c and Tables S7–S8, present the errors of multidimensional models under varying feature complexities (defined as the number of factors in the model). We observed that increasing feature complexity within the same dimension or increasing dimensionality at the same feature complexity reduced the root mean square error (RMSE) of the model. A lower RMSE indicates that the derived formula can more accurately predict outcomes based on the features. However, higher dimensionality and feature complexity usually increase the risk of overfitting. To evaluate model performance, we employed leave-one-out cross-validation (LOOCV).[46] Specifically, we iteratively selected one data point from the nine datasets as the test set, constructed the SISSO model using the remaining data, and then calculated the RMSE by applying the test data to the model. The average RMSE across all nine iterations yielded the LOOCV RMSE. As shown in Fig. 2d, the model with one dimension and a feature complexity of one exhibited the lowest LOOCV RMSE (0.181 eV), indicating superior predictive accuracy. This SISSO descriptor demonstrated strong correlation with $E_{bar}(Na_2S)$ ($R^2 = 0.855$) and low prediction error (RMSE = 0.094 eV), confirming its effectiveness in revealing the relationship between atomic physicochemical properties of C-SAMs and their catalytic performance (Fig. 2e and Table S9). The derived physical descriptor comprises only two features: the metallic radius (R_m) and covalent radius (R_c) of the metal atom. Analysis of the descriptor formula reveals that a smaller R_m or larger R_c of the C-SAM's metal atom leads to a lower $E_{bar}(Na_2S)$ on the C-SAM surface. Since all descriptor features are physical structural properties, they enable rapid prediction of C-SAM catalytic performance without requiring extensive computational resources.

Based on the above calculation results, we categorized C-SAMs into three categories according to their relative adsorption strengths for S and Na, and the $E_{bar}(Na_2S)$ is lower on S-

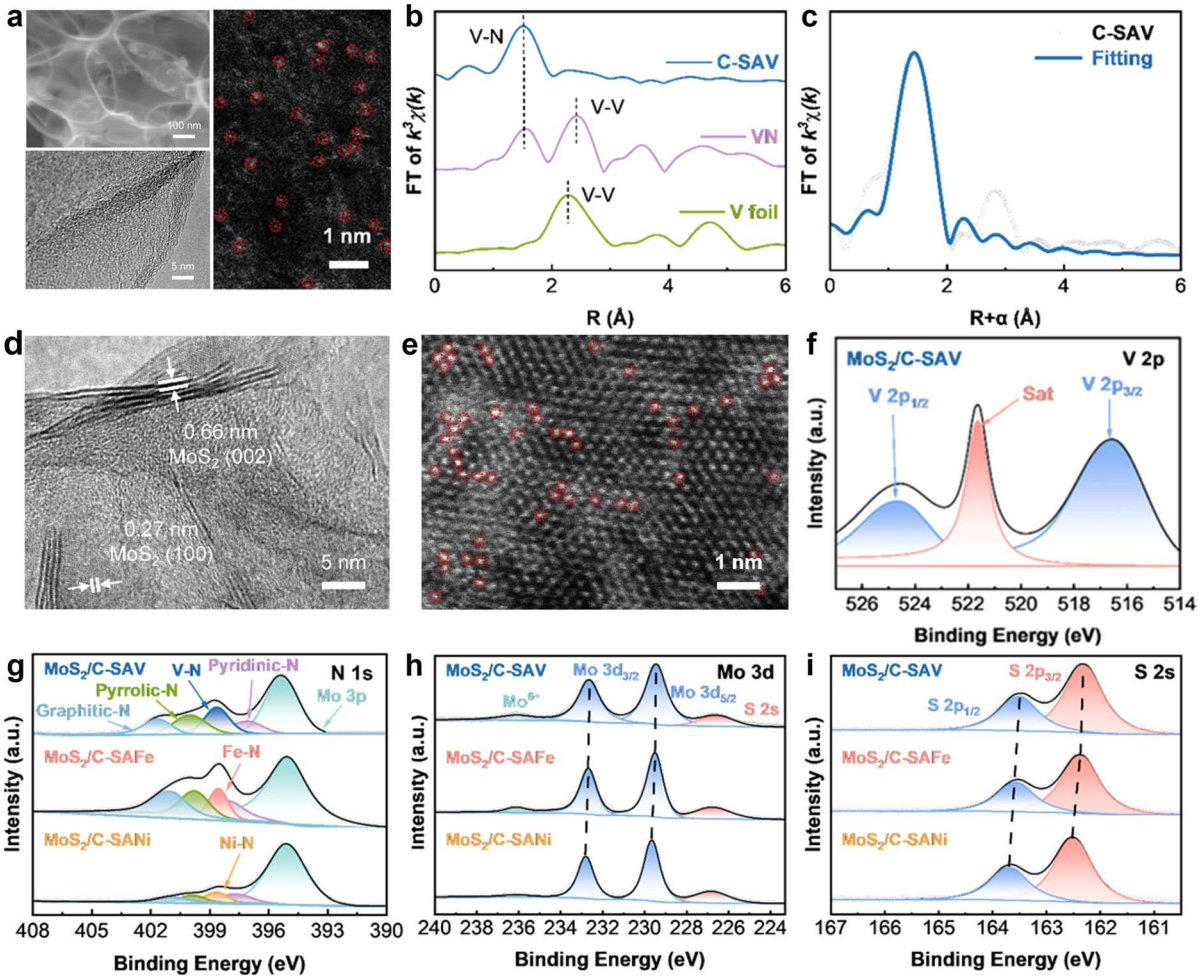

Fig. 3 (a) SEM images and TEM image of C-SAV. (b) FT-EXAFS of C-SAV. (c) EXAFS fitting of C-SAV. (d) TEM image of MoS_2/C-SAV. (e) AC-TEM image of MoS_2/C-SAV. (f) High-resolution XPS spectra of V for MoS_2/C-SAV. High-resolution XPS spectra of (g) N, (h) Mo, and (i) S for MoS_2/C-SAV, MoS_2/C-SAFe, and MoS_2/C-SANi.

affinitive C-SAMs, higher on Na-affinitive C-SAMs, and intermediate on amphiphilic C-SAMs. In particular, S-affinitive C-SAV exhibits the lowest barrier (0.989 eV), implying that coupling S-affinitive C-SAV with MoS_2 could facilitate its reversible structural transformation, thereby rendering it a promising anode candidate for SIBs.

To validate the reliability of the theoretical calculation, we employed the salt template method to synthesize three categories of catalysts: S-affinitive C-SAV, amphiphilic C-SAFe, and Na-affinitive C-SANi. As shown in scanning electron microscopy (SEM) images (Fig. 3a and S6), all three catalysts exhibit spherical porous network structures composed of uniformly sized pores. The thin carbon walls substantially increase the specific surface area of the catalyst, effectively mitigating the agglomeration of active species. High-resolution transmission electron microscopy (HRTEM) images further confirm the amorphous carbon structure of the catalysts (Fig. S7), with no obvious particles or clusters on the surface, indicating the absence of metal clusters or oxide. Spherical aberration-corrected scanning TEM annular dark-field (AC-STEM-ADF) images (Fig. 3a and S7) show that V, Fe, and Ni elements are successfully doped as single atoms and uniformly dispersed on the catalysts. The structural composition of the catalysts was systematically characterized using X-ray diffraction (XRD) and Raman spectroscopy. The XRD patterns (Fig. S8) reveal that all three samples only exhibit a characteristic peak at around 26° corresponding to the (002) plane of amorphous carbon, indicating that no metal clusters or crystalline oxides have been generated, which is consistent with the SEM and HR-TEM observations. Raman spectra show that the intensity ratios of the D-band to the G-band ($I_D : I_G$) for C-SAV, C-SAFe, and C-SANi catalysts are all substantially higher than 1, indicating the presence of abundant defects, which not only provide uniform anchoring sites for MoS_2 but also enhance the electronic interaction between the catalyst and MoS_2.

X-ray photoelectron spectroscopy (XPS) was further employed to investigate the chemical states of elements in the three catalysts. As shown in Fig. S9, the C–N peaks centered at 286.0 eV in C 1s spectra and the N-metal peaks centered at 397.5 eV in N 1s spectra confirm that the N atom is doped into the catalysts and located in the first coordination environment of the metal single atom. Fig. S10 presents the XPS spectra of V, Fe, and Ni elements, which display characteristic spin–orbit splitting peaks and corresponding satellite peaks, with binding energy positions matching those of metallic single-atom states, indicating that no metal oxides or clusters were formed. Furthermore, the chemical environments of metal single atoms were investigated by X-ray absorption spectroscopy (XAS) techniques. The spectra were compared with those of metal phthalocyanine (MPc), which features a distinctive $M–N_4$ structure, and metal foil. As shown in Fig. 3b and S11, the metal K-edge Fourier transform-extended X-ray absorption fine structure (FT-EXAFS) spectra exhibit a dominant peak at approximately 1.4–1.6 Å, which is attributed to the metal–N scattering path, and no metal–metal paths at 2.1–2.3 Å can be detected, suggesting that V, Fe, and Ni species are atomically dispersed in the catalysts. The FT-EXAFS spectra were fitted to determine the bond lengths and coordination information, as shown in Fig. 3c and S11; the V, Fe, and Ni atoms are all coordinated by four N atoms, with bond lengths of 1.98 Å (V–N), 2.02 Å (Fe–N), and 2.05 Å (Ni–N), respectively.

To investigate the effect of catalysts on the conversion reaction of MoS_2, MoS_2/C-SAM composites were synthesized *via* a solvothermal method. As shown in SEM images (Fig. S12), MoS_2 nanosheets are dispersed on the surfaces of the three catalysts without noticeable aggregation. This structure facilitates electrolyte infiltration and significantly reduces the transport pathway of Na^+, thereby enhancing ion conduction efficiency. HRTEM images (Fig. 3d and S13) show obvious lattice fringes with spacings of 0.66 nm and 0.27 nm, corresponding to the (002) and (100) planes of 2H-MoS_2, respectively, confirming the successful loading of MoS_2 on the C-SAM catalyst. Moreover, Fig. 3e and S13 present the AC-TEM images of the three composites, where bright spots corresponding to V, Fe, and Ni single atoms are uniformly distributed without agglomeration, indicating that the metal active sites remain atomically dispersed even after MoS_2 loading.

The electronic structure and phase composition of MoS_2/C-SAM were elucidated by XRD and Raman spectroscopy (Fig. S14), demonstrating the 2H phase structure of MoS_2. As shown in Fig. S14, the XRD patterns of all three composites exhibit excellent consistency with the standard 2H-MoS_2 (JCPDS PDF: 97-003-1067). The sharp and intense diffraction peaks of MoS_2 indicate its high crystallinity. The broad diffraction peak observed at around 26° can be attributed to the amorphous carbon. Raman spectra reveal characteristic peaks at 380.55 cm^{-1} and 405.19 cm^{-1}, corresponding to the in-plane $E_{2g}{}^1$ and out-of-plane $A_g{}^1$ vibrational modes of 2H-MoS_2, further confirming the successful preparation of 2H-MoS_2 in the composites. The chemical states of the three samples were characterized by XPS. The characteristic peaks of the three elements V, Fe, and Ni show no significant changes when compared with those of C-SAM catalysts (Fig. 3f and S15). The high-resolution C 1s and N 1s spectra (Fig. 3g and S16) clearly show the presence of C–N bonds and metal–N bonds, confirming that the N element is stably doped in the catalyst. The N 1s spectra show new characteristic peaks of Mo 3p, suggesting successful loading of MoS_2. These comprehensive spectroscopic analyses demonstrate that the structural integrity of the MN_4 active sites remains stable after loading MoS_2 nanosheets. To investigate the effect of the interaction between different catalysts and MoS_2 on the electronic structure of the samples, high-resolution Mo 3d and S 2p XPS spectra were further obtained, as shown in Fig. 3h–i. Concurrently, the theoretical calculation results (Fig. S17) also indicate that their binding energies exhibit downshifts from MoS_2/C-SANi, MoS_2/C-SAFe, to MoS_2/SAV, indicating that the C-SAV catalyst provides more electrons to MoS_2 and results in stronger hybridization, which is beneficial to improve the electrochemical performance of the MoS_2/C-SAV electrode.

To investigate the catalytic effects on the sodium storage performance of MoS_2, MoS_2/C-SAV, MoS_2/C-SAFe, and MoS_2/C-SANi were used as anode materials and sodium-ion half-cells were assembled. The rate performance of these cells was

evaluated through galvanostatic discharge/charge (GDC) measurements at current densities ranging from 0.1 to 5 A g^{-1}, as shown in Fig. 4a and S18. MoS_2/C-SAV exhibits superior specific capacities of 398.8, 391.0, 366.8, 353.7, 334.8, and 315.7 mAh g^{-1}, respectively, which are significantly higher than those of MoS_2/C-SAFe and MoS_2/C-SANi. When the current rate returns to 0.5 A g^{-1}, the specific capacity of MoS_2/C-SAV reaches 360.3 mAh g^{-1}, achieving 98.2% retention compared to its initial value at the same current density. The rate performance of MoS_2/C-SAV is significantly superior to that of most reported MoS_2-based anode materials for SIBs (Fig. 4b and Table S10).[47–53] The near-perfect overlap of GDC curves further confirms the rapid kinetic response and excellent reversible cycling reversibility of MoS_2/C-SAV.

The cycling performance was further examined at 5 A g^{-1}. As displayed in Fig. 4c, after activation, MoS_2/C-SAV exhibits a high specific capacity of 336.6 mAh g^{-1}. After 1000 cycles at 5 A g^{-1}, its discharge capacity remains at 332.8 mAh g^{-1}, which is much higher than those of MoS_2/C-SAFe (294.4 mAh g^{-1}) and MoS_2/C-SANi (271.1 mAh g^{-1}). The capacity retention rate of MoS_2/C-SAV is as high as 98.87%, corresponding to an ultralow capacity decay rate of merely 0.001% per cycle, indicating that the C-SAV catalyst effectively promotes the reversible conversion reaction of MoS_2 and endows MoS_2 with extremely long-cycle stability. The outstanding long-cycling performance of MoS_2/C-SAV is significantly better than that of most reported MoS_2-based anode materials for SIBs (Fig. 4d and Table S11).[12,37,47,51,54–57]

To gain deeper insights into the underlying mechanism of the superior Na^+ storage kinetics in MoS_2/C-SAV composites, *in situ* electrochemical impedance spectroscopy (EIS) and the galvanostatic intermittent titration technique (GITT) were employed. As shown in Fig. 4e, during the discharge process, as the voltage decreases from the open-circuit potential to 1.50 V, the R_{ct} values gradually increase due to the continuous adsorption of Na^+ ions on the electrode surface. After discharging below 1.50 V, the R_{ct} values exhibit a decreasing trend, which can be attributed to the phase transition from semiconducting 2H-MoS_2 to metallic 1T-Na_xMoS_2 upon Na^+ intercalation. The charging process exhibits symmetrical R_{ct} evolution, and subsequent cycles maintain stable low R_{ct} values, which not only confirms the highly reversible Na^+ storage mechanism but also demonstrates the superior charge transfer kinetics of MoS_2/C-SAV.

The Na^+ diffusion kinetics were investigated using the GITT (Fig. S19). The diffusion coefficient values of Na^+ (D_{Na^+}) could be calculated using the following equation:

$$D_{Na^+} = \frac{4L^2}{\pi\tau}\left(\frac{\Delta E_s}{\Delta E_t}\right)^2$$

where L represents the Na^+ diffusion length (cm), corresponding to the thickness of the electrode. t and τ represent the duration of the current pulse (s) and the relaxation time (s), respectively. ΔE_s denotes the steady-state potential change (V) by the current pulses and ΔE_t denotes potential change (V) during constant current pulses.

As shown in Fig. S19, MoS_2/C-SAV exhibits consistently higher Na^+ diffusion coefficients (D_{Na^+}) than MoS_2/C-SAFe and MoS_2/C-SANi during both charge and discharge processes, demonstrating that the C-SAV catalyst with strong S-atom adsorption capability effectively facilitates Na^+ diffusion

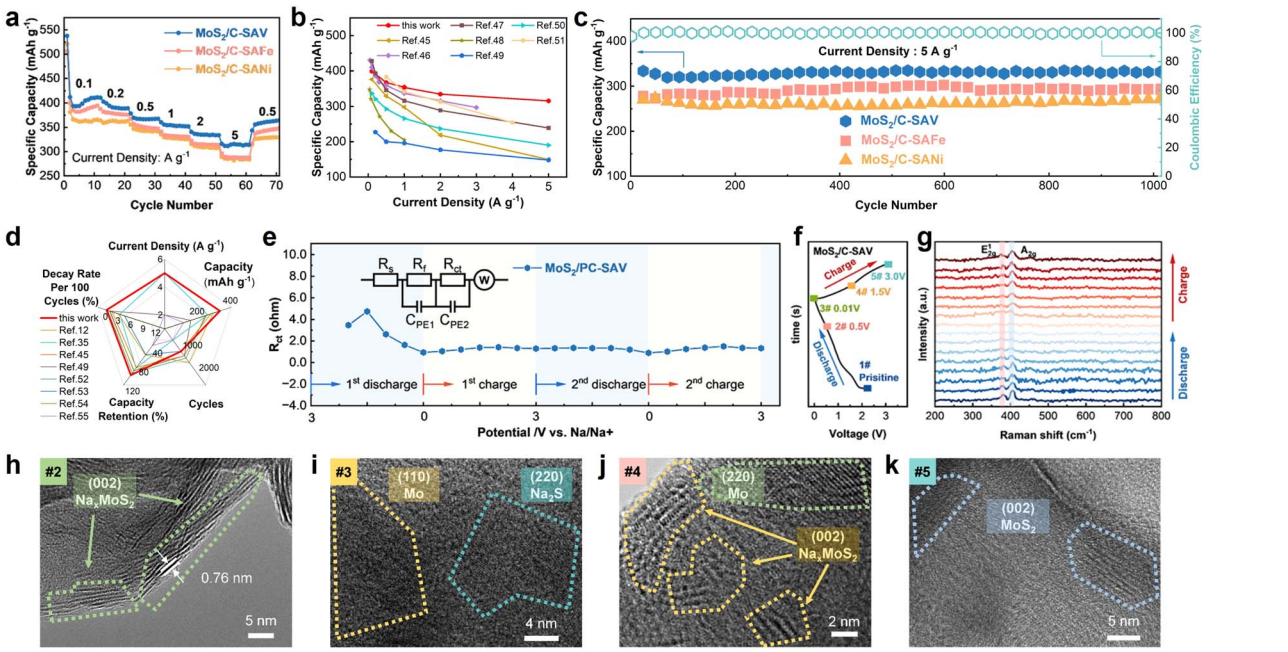

Fig. 4 (a) Rate performance of MoS_2/C-SAV, MoS_2/C-SAFe, and MoS_2/C-SANi. (b) Comparison of rate performances of MoS_2/C-SAV with that of the reported MoS_2-based anode materials for SIBs. (c) Long cycling performance of MoS_2/C-SAV, MoS_2/C-SAFe, and MoS_2/C-SANi. (d) Comparison of cycling performances of MoS_2/C-SAV with that of the reported MoS_2-based anode materials for SIBs. (e) The R_{ct} values of the 1st cycle and 2nd cycle for MoS_2/C-SAV. (f) GDC profiles and (g) corresponding *in situ* Raman spectra of MoS_2/C-SAV. *Ex situ* TEM images of MoS_2/C-SAV at different working states: (h) discharging at 0.50 V, (i) discharging at 0.01 V, (j) charging at 1.50 V, and (k) charging at 3.00 V.

kinetics of MoS_2. This conclusion is in excellent agreement with the observed electrochemical performance.

To elucidate the sodium storage mechanism of the MoS_2/C-SAV electrode, *in situ* Raman spectroscopy and *ex situ* TEM were employed to investigate the conversion process. The GDC profile in Fig. 4f shows five characteristic states corresponding to distinct phase transitions during the sodium storage process: (1) initial pristine state, (2) discharged to 0.50 V, (3) fully discharged to 0.01 V, (4) charged to 1.50 V, and (5) fully charged to 3.00 V. Fig. 4g presents the *in situ* Raman spectroscopy spectra of the MoS_2/C-SAV electrode. Before cycling, distinct characteristic peaks corresponding to the in-plane E_{2g}^1 and out-of-plane A_g^1 vibrational modes of MoS_2 are observed. During the discharge process, the intensity of MoS_2 characteristic peaks progressively weakens with decreasing voltage, suggesting the gradual conversion of MoS_2 into the discharge products Mo and Na_2S. Upon complete discharge to 0.01 V, the MoS_2 peaks disappear completely. During the subsequent charging process, the MoS_2 peaks reappear and their intensity gradually recovers with the increase of voltage. After one complete cycle, the peak intensity of MoS_2 nearly returns to its initial level, confirming the highly reversible conversion reaction of MoS_2 in MoS_2/C-SAV.

The structural evolution and compositional changes of MoS_2/C-SAV during cycling were further elucidated through *ex situ* TEM. As illustrated in Fig. 4h–k, when discharging to 0.50 V, the TEM image reveals distinct lattice fringes with *a* spacing of 0.74 nm, corresponding to the (002) plane of $NaMoS_2$, confirming the successful intercalation of Na^+ into MoS_2 interlayers and the formation of the intermediate $NaMoS_2$ phase.

When discharging to 0.01 V, the $NaMoS_2$ lattice fringes completely disappear, while new lattice spacings of 0.30 nm and 0.22 nm emerge, corresponding to the (220) plane of Na_2S and the (110) plane of metallic Mo, respectively, indicating complete conversion to the final discharge products. During the subsequent charging process, when the voltage returns to 1.50 V, the (002) lattice fringes of $NaMoS_2$ reappear. Upon reaching 3.00 V, abundant lattice fringes with 0.62 nm spacing are clearly observed, matching the (002) plane of MoS_2. These results demonstrate that S-affinitive catalyst C-SAV effectively facilitates the reversible conversion reaction, thereby endowing the MoS_2/C-SAV electrode with high electrochemical reversibility and structural stability.

Conclusions

In summary, we propose classifying C-SAMs into three categories based on their adsorption strength and relative affinity for S and Na: S-affinitive C-SAMs, amphiphilic C-SAMs, and Na-affinitive C-SAMs. Using first-principles calculations, we investigated their effects on catalyzing Na_2S decomposition and reaction reversibility. Our findings reveal that S-affinitive C-SAMs weaken the Na–S bond in Na_2S through strong adsorption, facilitating its cleavage during charging and thereby reducing the $E_{bar}(Na_2S)$ on the C-SAMs surface. Based on these results, we propose the following design principles for C-SAMs to promote the reversible conversion of MoS_2: firstly, C-SAMs should form strong hybridization with S to enhance adsorption. Secondly, the adsorption of Na should be moderated to avoid excessive binding that could hinder Na^+ desorption. This approach ensures efficient Na_2S decomposition without compromising Na^+ desorption, thereby promoting reversible charging. Subsequently, we experimentally validated these speculations using S-affinitive C-SAV, amphiphilic C-SAFe, and Na-affinitive C-SANi as examples. Through *in situ* and *ex situ* characterization at different stages of battery cycling, we demonstrated that the S-affinitive catalyst C-SAV significantly enhances the reaction kinetics of MoS_2 for Na^+ storage, facilitating a highly reversible conversion reaction during charging ($Mo/Na_2S \rightarrow NaMoS_2 \rightarrow MoS_2$). This property endows MoS_2 with exceptional reversibility in SIBs. Moreover, compared to Na-affinitive and amphiphilic C-SAMs, the composite electrode formed by the S-affinitive C-SAMs and MoS_2 exhibits superior electrochemical performance. After 1000 cycles at a high current density of 5 A g^{-1}, the MoS_2/C-SAV electrode exhibits a specific capacity of 332.8 mAh g^{-1} with a capacity retention rate of 98.87%, corresponding to an average capacity decay of only 0.001% per cycle.

Author contributions

T. W. conceived the idea and designed the project. T. W., Q. Z. and N. W. supervised the work and revised the paper. K. C. and Z. Q. conducted the concept design, analyzed the results and drafted the manuscript. K. C., Z. Q., W. Z., and B. C. prepared the electrode materials and tested the performance. K. C. and D. L. contributed to the calculation parts. All authors commented on the final manuscript and discussed the results.

Conflicts of interest

There are no conflicts to declare.

Data availability

The data supporting this article have been included as part of the supplementary information (SI). Supplementary information: experimental section (materials, characterization, and electrochemical measurements), computational methods, and supporting figures including electrochemical performances, SEM, TEM, XRD, XPS, and FT-EXAFS characterization, and tables. See DOI: https://doi.org/10.1039/d5sc08906a.

Acknowledgements

This work was financially supported by the Natural Science Basic Research Program of Shaanxi (Program No. 2024JC-YBQN-0073), the Natural Science Foundation of Chongqing (No. CSTB2023NSCQ-MSX0538), the Natural Science Foundation of Tianjin City (23JCZDJC01110), the Fundamental Research Funds for the Central Universities (No. G2025KY06151), and the Young Talent Fund of Association for Science and Technology in Shaanxi (No. 20230101). DL acknowledges the project e-

INFRA CZ (ID: 90254) of the Ministry of Education, Youth and Sports of the Czech Republic.

Notes and references

1 J. Li, D. Röhrens, G. Dalfollo, X. Wu, Z. Lu, Q. Gao, B. Han, R. Sun, C. Zhou, J. Wang and Z. Cai, Low-Temperature Replacement Construction of Three-Dimensional Corrosion-Resistant Interface for Deeply Rechargeable Zn Metal Batteries, *Nano Mater. Sci.*, 2024, **6**, 329–336.

2 L. Li, Y. Zheng, S. Zhang, J. Yang, Z. Shao and Z. Guo, Recent Progress on Sodium Ion Batteries: Potential High-Performance Anodes, *Energy Environ. Sci.*, 2018, **11**, 2310–2340.

3 X. Yang and A. L. Rogach, Anodes and Sodium-Free Cathodes in Sodium Ion Batteries, *Adv. Energy Mater.*, 2020, **10**, 2000288.

4 S. Gan, Y. Huang, N. Hong, Y. Zhang, B. Xiong, Z. Zheng, Z. He, S. Gao, W. Deng, G. Zou, H. Hou and X. Ji, Comprehensive Understanding of Closed Pores in Hard Carbon Anode for High-Energy Sodium-Ion Batteries, *Nano-Micro Lett.*, 2025, **17**, 325.

5 N. LeGe, Y.-H. Zhang, W.-H. Lai, X.-X. He, Y.-X. Wang, L.-f. Zhao, M. Liu, X. Wu and S.-L. Chou, Potassium Escaping Balances the Degree of Graphitization and Pore Channel Structure in Hard Carbon to Boost Plateau Sodium Storage Capacity, *Chem. Sci.*, 2025, **16**, 1179–1188.

6 S. Li, J. Zhang, Y. Li, P. Fan and M. Wu, Revisiting N, S Co-Doped Carbon Materials with Boosted Electrochemical Performance in Sodium-Ion Capacitors: The Manipulation of Internal Electric Field, *Nano Res. Energy*, 2024, **3**, e9120098.

7 Y. Wan, Y. Liu, D. Chao, W. Li and D. Zhao, Recent Advances in Hard Carbon Anodes with High Initial Coulombic Efficiency for Sodium-Ion Batteries, *Nano Mater. Sci.*, 2023, **5**, 189–201.

8 S. Awasthi, S. Moharana, V. Kumar, N. Wang, E. Chmanehpour, A. D. Sharma, S. K. Tiwari, V. Kumar and Y. K. Mishra, Progress in Doping and Crystal Deformation for Polyanions Cathode Based Lithium-Ion Batteries, *Nano Mater. Sci.*, 2024, **6**, 504–535.

9 J. Wang, J. Zhang, X. Cheng, Y. Zhang, H. Li, Q. Guan, F. Wu, H. Li, D. Wang, M. Liu, Y. Zhang, Q. Xiao, S. Passerini and H. Lin, Electrode/Electrolyte Interface Studies of Rechargeable Li Batteries with Interface-Specific Sum Frequency Generation Spectroscopy, *J. Am. Chem. Soc.*, 2025, **147**, 44633–44651.

10 Y. Liu, C. Yang, Q. Zhang and M. Liu, Recent Progress in the Design of Metal Sulfides as Anode Materials for Sodium Ion Batteries, *Energy Storage Mater.*, 2019, **22**, 66–95.

11 Y. Gao, H. Zhang, J. Peng, L. Li, Y. Xiao, L. Li, Y. Liu, Y. Qiao and S.-L. Chou, A 30-year Overview of Sodium-Ion Batteries, *Carbon Energy*, 2024, **6**, e464.

12 H. Xie, B. Chen, C. Liu, G. Wu, S. Sui, E. Liu, G. Zhou, C. He, W. Hu and N. Zhao, Engineering the Interfacial Doping of 2D Heterostructures with Good Bidirectional Reaction Kinetics for Durably Reversible Sodium-Ion Batteries, *Energy Storage Mater.*, 2023, **60**, 102830.

13 F. Kang, L. Yan, Y. Cao, Z. Chen, Y. Zhao, X. Wang, Y. Zhang, L. Cheng, Q. Gu, J. Yang, F.-R. Chen, C.-S. Lee, Y. Wang and Q. Zhang, Poly(p-benzoquinono)diimidazole-Linked Covalent Organic Framework as an Efficient Anode Endues Sodium-Ion Batteries with High Performance and Wide Temperature Adaptability, *J. Am. Chem. Soc.*, 2025, **147**, 26069–26078.

14 S. Tao, Z. Cao, X. Xiao, Z. Song, D. Xiong, Y. Tian, W. Deng, Y. Liu, H. Hou, G. Zou and X. Ji, Tunable Platform Capacity of Metal-Organic Frameworks *via* High-Entropy Strategy for Ultra-Fast Sodium Storage, *Nano-Micro Lett.*, 2025, **17**, 201.

15 T. Wang, J. Xiao, X. Cao, Y. Fan and Q. Zhang, Interface Effect on Promoting Reversible Conversion for Na_2Se in the Metal Selenide as Sodium Ion Batteries, *J. Energy Chem.*, 2020, **44**, 8–12.

16 T. Wang, D. Legut, Y. Fan, J. Qin, X. Li and Q. Zhang, Building Fast Diffusion Channel by Constructing Metal Sulfide/Metal Selenide Heterostructures for High-Performance Sodium Ion Batteries Anode, *Nano Lett.*, 2020, **20**, 6199–6205.

17 T. Wang, J. Qu, D. Legut, J. Qin, X. Li and Q. Zhang, Unique Double-Interstitialcy Mechanism and Interfacial Storage Mechanism in the Graphene/Metal Oxide as the Anode for Sodium-Ion Batteries, *Nano Lett.*, 2019, **19**, 3122–3130.

18 X. Wang, X. Shen, Z. Wang, R. Yu and L. Chen, Atomic-Scale Clarification of Structural Transition of MoS_2 upon Sodium Intercalation, *ACS Nano*, 2014, **8**, 11394–11400.

19 T. Liu, Y. Wang, J. Zhou, G. Wu, B. Chen, G. Zhou, F. He, C. He, W. Hu, N. Zhao and N. Wu, Revealing the Design Principle for Highly Compositional Reversible Transition Metal Chalcogenide Electrodes: A Perspective, *Adv. Mater.*, 2025, e14760, DOI: 10.1002/adma.202514760.

20 Q. Q. Li, Z. P. Yao, J. S. Wu, S. Mitra, S. Q. Hao, T. S. Sahu, Y. Li, C. Wolverton and V. P. Dravid, Intermediate Phases in Sodium Intercalation into MoS_2 Nanosheets and their Implications for Sodium-Ion Batteries, *Nano Energy*, 2017, **38**, 342–349.

21 L. Habib, G. Suo, C. Lin, J. Li, S. Javed, K. Naseem and Z. K. Kalkozova, Strategies in Improving the Initial Coulombic Efficiency of Transition Metal Chalcogenides Anode Materials for Sodium-Ion Batteries: A Review, *Renewable Sustainable Energy Rev.*, 2025, **217**, 115721.

22 Y. Xiao, S. H. Lee and Y.-K. Sun, The Application of Metal Sulfides in Sodium Ion Batteries, *Adv. Energy Mater.*, 2017, **7**, 1601329.

23 B. Chen, T. Wang, S. Zhao, J. Tan, N. Zhao, S. P. Jiang, Q. Zhang, G. Zhou and H.-M. Cheng, Efficient Reversible Conversion between MoS_2 and Mo/Na_2S Enabled by Graphene-Supported Single Atom Catalysts, *Adv. Mater.*, 2021, **33**, 2007090.

24 Y.-J. Lei, X. Lu, H. Yoshikawa, D. Matsumura, Y. Fan, L. Zhao, J. Li, S. Wang, Q. Gu, H.-K. Liu, S.-X. Dou, S. Devaraj, T. Rojo, W.-H. Lai, M. Armand, Y.-X. Wang and G. Wang, Understanding the Charge Transfer Effects of

Single Atoms for Boosting the Performance of Na-S Batteries, *Nat. Commun.*, 2024, **15**, 3325.

25 C. Liu, H. Xie, S. Sui, B. Chen, L. Ma, E. Liu and N. Zhao, Interface Engineering of MoS_2-Based Ternary Hybrids towards Reversible Conversion of Sodium Storage, *Mater. Today Energy*, 2022, **26**, 100993.

26 X. Wu, X. Yu, Z. Tian, X. Yang and J. Xu, Carbonaceous Catalyst Boosting Conversion Kinetics of Na_2S in Na-Ion Batteries, *Energy Storage Mater.*, 2025, **74**, 103899.

27 X.-L. Huang, X. Li, L. Zhao, L. Yao, K. Zhu, W.-H. Lai, Y.-X. Wang and H.-K. Liu, Manipulating Sulfur Redox Kinetics in Rechargeable Metal-Sulfur Batteries: Fundamental Principles and Universal Methodologies, *Adv. Mater.*, 2025, **37**, 2419089.

28 P. Li, Y. Yang, S. Gong, F. Lv, W. Wang, Y. Li, M. Luo, Y. Xing, Q. Wang and S. Guo, Co-doped 1T-MoS_2 Nanosheets Embedded in N, S-Doped Carbon Nanobowls for High-Rate and Ultra-Stable Sodium-Ion Batteries, *Nano Res.*, 2019, **12**, 2218–2223.

29 Y. Zhang, B. Han, S. Tan, Q. Gao, Z. Cai, C. Zhou, J. Li, R. Sun and K. Amine, Interfacial Engineering of Metal Chalcogenides-based Heterostructures for Advanced Sodium-Ion Batteries, *Adv. Energy Mater.*, 2025, **15**, 2404796.

30 C. L. Liu, Y. Bai, Y. Zhao, H. Yao and H. Pang, MoS_2/Graphene Composites: Fabrication and Electrochemical Energy Storage, *Energy Storage Mater.*, 2020, **33**, 470–502.

31 T. Wang, S. Chen, H. Pang, H. Xue and Y. Yu, MoS_2-Based Nanocomposites for Electrochemical Energy Storage, *Adv. Sci.*, 2017, **4**, 1600289.

32 S. Sui, H. Xie, B. Chen, T. Wang, Z. Qi, J. Wang, J. Sha, E. Liu, S. Zhu, K. Lei, S. Zheng, G. Zhou, C. He, W. Hu, F. He and N. Zhao, Highly Reversible Sodium-ion Storage in A Bifunctional Nanoreactor Based on Single-atom Mn Supported on N-doped Carbon over MoS_2 Nanosheets, *Angew. Chem., Int. Ed.*, 2024, **63**, e202411255.

33 J. Wang, T. Liu, B. Chen, Z. Qi, H. Xie, G. Wu, L. Xiao, J. Zhou, L. Ma, F. He, C. He, W. Hu and N. Zhao, Engineering the Catalytic Superlattices for Highly Reversible Sodium-Ion Storage with A High Compositional Conversion Degree, *Angew. Chem., Int. Ed.*, 2025, **64**, e202425063.

34 X. Wen, W. Feng, X. Li, J. Yang, R. Du, P. Wang, H. Li, L. Song, Y. Wang, M. Cheng, J. He and J. Shi, Diatomite-Templated Synthesis of Single-Atom Cobalt-Doped MoS_2/Carbon Composites to Boost Sodium Storage, *Adv. Mater.*, 2023, **35**, 2211690.

35 Z. Han, S. Zhao, J. Xiao, X. Zhong, J. Sheng, W. Lv, Q. Zhang, G. Zhou and H. M. Cheng, Engineering d-p Orbital Hybridization in Single-Atom Metal-Embedded Three-Dimensional Electrodes for Li-S Batteries, *Adv. Mater.*, 2021, **33**, 2105947.

36 Y. Jiang, Z. Yu, X. Zhou, X. Cheng, H. Huang, F. Liu, Y. Yang, S. He, H. Pan, H. Yang, Y. Yao, X. Rui and Y. Yu, Single-Atom Vanadium Catalyst Boosting Reaction Kinetics of Polysulfides in Na-S Batteries, *Adv. Mater.*, 2023, **35**, e2208873.

37 H. Tian, Y. Lei, B. Sun, C.-C. Yang, C.-L. Chen, T. Huang, X. Zhang, Y. Chen, A. Song, L. Pang, H. Wang, C.-L. Dong, S. C. Smith, W.-H. Lai, Y.-X. Wang, X. Tan, H. Liu and G. Wang, p-d Orbital Hybridization Induced by Transition Metal Atom Sites for Room-Temperature Sodium-Sulfur Batteries, *Natl. Sci. Rev.*, 2025, **12**, nwaf241.

38 G. Wu, T. Liu, Z. Lao, Y. Cheng, T. Wang, J. Mao, H. Zhang, E. Liu, C. Shi, G. Zhou, C. He, W. Hu, N. Zhao, N. Wu and B. Chen, Optimizing s-p Orbital Overlap Between Sodium Polysulfides and Single-Atom Indium Catalyst for Efficient Sulfur Redox Reaction, *Angew. Chem., Int. Ed.*, 2025, **64**, e202422208.

39 Y. Wang, J. Shen, J. Sun, J. Xu, B. Huang, T. Wang and T. Zhao, Role of s-p Orbital Hybridization in Enhancing the Lithium-Ion Conductivity of Antiperovskite $Li_{3-x}OH_xCl$ Solid Electrolytes, *ACS Energy Lett.*, 2025, **10**, 3655–3662.

40 Z. Qi, K. Cui, S. Sui, Y. Wang, H. Xie, G. Wu, Y. Cheng, E. Liu, F. He, C. He, T. Wang, B. Chen and N. Zhao, Regulating the Orbital Hybridization to Induce Asymmetrical Catalysis for Efficient Reversible Sodium Conversion Storage, *Sci. China Mater.*, 2025, **68**, 3277–3287.

41 Z. Qiao, R. Jiang, H. Xu, D. Cao and X. C. Zeng, A General Descriptor for Single-Atom Catalysts with Axial Ligands, *Angew. Chem., Int. Ed.*, 2024, **63**, e202407812.

42 C. He, C.-H. Lee, L. Meng, H.-Y. T. Chen and Z. Li, Selective Orbital Coupling: An Adsorption Mechanism in Single-Atom Catalysis, *J. Am. Chem. Soc.*, 2024, **146**, 12395–12400.

43 Z. Han, S. Tao, Y. Jia, M. Zhang, R. Ma, X. Xiao, J. Zhou, R. Gao, K. Cui, T. Wang, X. Zhang and G. Zhou, Data-Driven Insight into the Universal Structure-Property Relationship of Catalysts in Lithium-Sulfur Batteries, *J. Am. Chem. Soc.*, 2025, **147**, 22851–22863.

44 K. Cui, T. Wang, Q. Zhang and H. Zhang, Multi-Functional Descriptor Design of V-Based Double Atomic Catalysts for Room Temperature Sodium-Sulfur Batteries, *Small*, 2025, **21**, 2409866.

45 R. Ouyang, S. Curtarolo, E. Ahmetcik, M. Scheffler and L. M. Ghiringhelli, SISSO: A Compressed-Sensing Method for Identifying the Best Low-Dimensional Descriptor in an Immensity of Offered Candidates, *Phys. Rev. Mater.*, 2018, **2**, 083802.

46 J. Wang, H. Xie, Y. Wang and R. Ouyang, Distilling Accurate Descriptors from Multi-Source Experimental Data for Discovering Highly Active Perovskite OER Catalysts, *J. Am. Chem. Soc.*, 2023, **145**, 11457–11465.

47 S. Sui, H. Xie, M. Liang, B. Chen, C. Liu, E. Liu, B. Chen, L. Ma, J. Sha and N. Zhao, Three-in-One" Multi-Level Design of MoS_2-Based Anodes for Enhanced Sodium Storage: from Atomic to Macroscopic Level, *Adv. Funct. Mater.*, 2022, **32**, 2110853.

48 Y. Fang, D. Luan, Y. Chen, S. Gao and X. W. Lou, Rationally Designed Three-Layered Cu_2S@Carbon@MoS_2 Hierarchical Nanoboxes for Efficient Sodium Storage, *Angew. Chem., Int. Ed.*, 2020, **59**, 7178–7183.

49 H. Pan, Y. Huang, X. Cen, M. Zhang, J. Hou, C. Wu, Y. Dou, B. Sun, Y. Wang, B. Zhang and L. Zhang, Hollow Carbon and MXene Dual-Reinforced MoS_2 with Enlarged Interlayers for High-Rate and High-Capacity Sodium Storage Systems, *Adv. Sci.*, 2024, **11**, 2400364.

50 X. Xie, T. Makaryan, M. Zhao, K. L. Van Aken, Y. Gogotsi and G. Wang, MoS_2 Nanosheets Vertically Aligned on Carbon Paper: A Freestanding Electrode for Highly Reversible Sodium-Ion Batteries, *Adv. Energy Mater.*, 2016, **6**, 1502161.
51 Y.-L. Ding, P. Kopold, K. Hahn, P. A. van Aken, J. Maier and Y. Yu, A Lamellar Hybrid Assembled from Metal Disulfide Nanowall Arrays Anchored on a Carbon Layer: *In Situ* Hybridization and Improved Sodium Storage, *Adv. Mater.*, 2016, **28**, 7774–7782.
52 T. Wang, K. Yao, Y. Hua, E. G. Shankar, R. Shanthappa and J. S. Yu, Rational Design of MXene-MoS_2 Heterostructure with Rapid Ion Transport Rate as an Advanced Anode for Sodium-Ion Batteries, *Chem. Eng. J.*, 2023, **457**, 141363.
53 K. Zhu, S. Gao, T. Bai, H. Li, X. Zhang, Y. Mu, W. Guo, Z. Cui, N. Wang and Y. Zhao, Heterogeneous MoS_2 Nanosheets on Porous TiO_2 Nanofibers toward Fast and Reversible Sodium-Ion Storage, *Small*, 2024, **20**, 2402774.
54 P. Li, J. Y. Jeong, B. Jin, K. Zhang and J. H. Park, Vertically Oriented MoS_2 with Spatially Controlled Geometry on Nitrogenous Graphene Sheets for High-Performance Sodium-Ion Batteries, *Adv. Energy Mater.*, 2018, **8**, 1703300.
55 C. Cui, Z. Wei, J. Xu, Y. Zhang, S. Liu, H. Liu, M. Mao, S. Wang, J. Ma and S. Dou, Three-Dimensional Carbon Frameworks Enabling MoS_2 as Anode for Dual Ion Batteries with Superior Sodium Storage Properties, *Energy Storage Mater.*, 2018, **15**, 22–30.
56 Y. Xia, T. Yang, Z. Wang, T. Mao, Z. Hong, J. Han, D.-L. Peng and G. Yue, Van der Waals Forces between S and P Ions at the CoP-C@MoS_2/C Heterointerface with Enhanced Lithium/Sodium Storage, *Adv. Funct. Mater.*, 2023, **33**, 2302830.
57 Y. Li, H. Wang, L. Wang, R. Wang, B. He, Y. Gong and X. Hu, Ultrafast Na^+-Storage in TiO_2-Coated MoS_2@N-Doped Carbon for High-Energy Sodium-Ion Hybrid Capacitors, *Energy Storage Mater.*, 2019, **23**, 95–104.